

Persistence Spheres: Bi-Continuous Representations of Persistence Diagrams.

Matteo Pegoraro*

September 23, 2025

Abstract

We introduce persistence spheres, a novel functional representation of persistence diagrams. Unlike existing embeddings—such as persistence images, landscapes, or kernel methods—persistence spheres provide a bi-continuous mapping: they are Lipschitz continuous with respect to the 1-Wasserstein distance and admit a continuous inverse on their image. This ensures, in a theoretically optimal way, both stability and geometric fidelity, making persistence spheres the representation that most closely mirrors the Wasserstein geometry of PDs in linear space. We derive explicit formulas for persistence spheres, showing that they can be computed efficiently and parallelized with minimal overhead. Empirically, we evaluate them on diverse regression and classification tasks involving functional data, time series, graphs, meshes, and point clouds. Across these benchmarks, persistence spheres consistently deliver state-of-the-art or competitive performance compared to persistence images, persistence landscapes, and the sliced Wasserstein kernel.

Keywords: Topological Data Analysis, Persistence Diagrams, Lift Zonoid, Vectorization, Topological Machine Learning

1. Introduction

Topological Data Analysis (TDA) is an emerging field that leverages concepts from algebraic topology to study the shape of data, offering coordinate-free and noise-robust methods for extracting meaningful patterns. At the core of TDA lies persistent homology, a framework that captures multi-scale topological features of a dataset. By recording the scales at which features such as connected components, loops, and voids appear (birth) and disappear (death), persistent homology produces compact descriptors of data shape. These descriptors are commonly represented as persistence diagrams (PDs) or barcodes, which provide stable and interpretable summaries amenable to qualitative exploration and (limited) quantitative analysis (Edelsbrunner and Harer, 2010; Oudot, 2015).

Data Analysis with Persistence Diagrams. To integrate topological information into data analysis pipelines, PDs are often compared using Wasserstein distances defined through partial optimal transport (POT) (Divol and Lacombe, 2021). These distances play a crucial role in ensuring robustness to perturbations, but they also impose a highly non-linear geometry on the space of PDs. This non-linearity significantly limits the range of statistical tools that can be directly applied to PDs. For instance, even basic operations such as computing averages are non-trivial: they are usually formulated in terms of Wasserstein barycenters (Mileyko et al., 2011), which are computationally intensive to approximate and may fail to yield unique solutions.

*. Department of Mathematics, KTH

Topological Machine Learning: Vectorizations and Kernel Methods. To overcome these limitations, numerous vectorization methods have been developed to embed PDs into linear spaces, enabling the use of classical statistical and machine learning techniques. Such embeddings underpin the field of *topological machine learning* (Papamarkou et al., 2024), where topological features and topological loss functions have proven effective in both predictive and representation learning tasks (Moor et al., 2020; Wayland et al., 2024). For comprehensive surveys we refer to Pun et al. (2022); Ali et al. (2023); Papamarkou et al. (2024); here we only recall the main approaches.

Broadly, these methods fall into two main categories. The first consists of explicit embeddings of PDs into linear spaces, while the second comprises kernel methods (Reininghaus et al., 2015; Kusano et al., 2018; Carriere et al., 2017), which employ the *kernel trick* to define feature maps implicitly. Within the class of explicit embeddings, one can further distinguish between approaches based on *descriptive statistics* (Asaad et al., 2022), *algebraic representations* exploiting polynomial rings or tropical coordinates (Kališnik, 2019; Monod et al., 2019; Di Fabio and Ferri, 2015), *functional representations*, which associate to each diagram a scalar field over a chosen domain (Bubenik, 2015; Adams et al., 2017; Biscio and Møller, 2019; Gotovac Dogaš and Mandarić, 2025) and other approaches (Mitra and Virk, 2024).

Main Contributions. In this work, we build on the framework of Gotovac Dogaš and Mandarić (2025) (see Remark 2) and propose a new functional representation of PDs, mapping a diagram D to a function $\varphi : \mathbb{S}^2 \rightarrow \mathbb{R}$. We show that this mapping is Lipschitz continuous with respect to the 1-Wasserstein distance between diagrams, and that its inverse—on its domain of definition—is also continuous. Continuity of the forward map guarantees stability, since similar diagrams yield similar functions, while continuity of the inverse ensures that functional similarity always corresponds to similarity between diagrams. Crucially, this bi-continuity establishes the strongest possible geometric correspondence between the Wasserstein space of PDs and their functional representation, given that a bi-Lipschitz embedding is known to be impossible (Carrière and Bauer, 2019). To the best of our knowledge, no other vectorization of PDs combines these properties. Stronger guarantees can only be obtained by restricting attention to diagrams with at most n points, for some fixed n , as in Mitra and Virk (2024).

2. Preliminaries

2.1 Convex Sets and Support Functions

We briefly review the notation and concepts from convex analysis and geometry that will be used throughout. Standard references include Rockafellar (1997); Salinetti and Wets (1979).

Definition 1 *Given two convex sets $A, B \subset \mathbb{R}^2$, their Minkowski sum and their multiplication with a non-negative scalar $\lambda \geq 0$, are defined as:*

$$A \oplus B = \{a + b \mid a \in A, b \in B\}, \lambda A = \{\lambda a \mid a \in A\}.$$

Definition 2 *Given a compact convex set $A \subset \mathbb{R}^2$, its support function is defined as:*

$$\begin{aligned} h_A : \mathbb{R}^2 &\rightarrow \mathbb{R} \\ x &\mapsto \max_{a \in A} \langle x, a \rangle. \end{aligned}$$

One can check that 1) any support function is completely determined by its restriction on \mathbb{S}^2 ; 2) the operator $A \mapsto h_A$ is linear: $\lambda_1 A \oplus \lambda_2 B \mapsto \lambda_1 h_A + \lambda_2 h_B$.

To compare different convex sets we will use the Hausdorff distance.

Definition 3 *Given two compact subsets $A, B \subset Z$, with (Z, d_Z) being a metric space, their Hausdorff distance is defined as:*

$$d_H(A, B) = \max\{\max_{a \in A} d_Z(a, B), \max_{b \in B} d_Z(b, A)\}$$

Now we can state the following classical result.

Proposition 1 *Given two compact convex sets $A, B \subset \mathbb{R}^2$, the following holds:*

$$\max_{v \in \mathbb{S}^2} \|h_A(v) - h_B(v)\|_2 = d_H(A, B).$$

In particular, the operator $A \mapsto h_A$ is injective.

2.2 Integrable Measures on \mathbb{R}^2

For any Borel measure μ on \mathbb{R}^2 , and any $f : \mathbb{R}^2 \rightarrow \mathbb{R}$ μ -measurable, we set:

$$\langle \mu, f \rangle := \int_{\mathbb{R}^2} f(p) d\mu(p).$$

Moreover, for any $r \geq 0$, we set $B_r = \{p \in \mathbb{R}^2 \mid \|p\|_2 \leq r\}$, and $B_r^c = \mathbb{R}^2 \setminus B_r$.

In the following we will use *integrable* measures and *uniformly* integrable sequences of measures. See Hendrych and Nagy (2022) for more details on such topics.

Definition 4 *A positive finite Borel measure on \mathbb{R}^2 , μ , is called integrable if:*

$$\langle \mu, \|\cdot\|_2 \rangle = \int_{\mathbb{R}^2} \|p\|_2 d\mu(p) < \infty.$$

Similarly, a sequence of integrable measures $\{\mu_n\}_{n \in \mathbb{N}}$ is uniformly integrable if:

$$\lim_{r \rightarrow \infty} \sup_{n \in \mathbb{N}} \int_{B_r^c} \|p\|_2 d\mu_n(p) = 0.$$

To compare measures, we need weak and vague convergence of measures, which are standard notions in measure theory. See, for instance, Kallenberg (1997).

Definition 5 *A sequence of integrable measures $\{\mu_n\}_{n \in \mathbb{N}}$ converges weakly to μ if $\langle \mu_n, f \rangle \rightarrow \langle \mu, f \rangle$ for every $f : \mathbb{R}^2 \rightarrow \mathbb{R}$ continuous and bounded. Instead, if $\langle \mu_n, f \rangle \rightarrow \langle \mu, f \rangle$ for every $f : \mathbb{R}^2 \rightarrow \mathbb{R}$ continuous and compactly supported, we say that $\{\mu_n\}_{n \in \mathbb{N}}$ converges vaguely to μ .*

We write $\mu_n \xrightarrow{w} \mu$ for weak convergence and $\mu_n \xrightarrow{v} \mu$ for vague convergence.

2.3 Persistence Diagrams

We adopt a measure-theoretic perspective to define PDs. First, we introduce the following notation:

$$\mathbb{R}_{x < y}^2 := \{(x, y) \in \mathbb{R}^2 \mid x < y\}, \quad \Delta := \{(x, y) \in \mathbb{R}^2 \mid x = y\}.$$

Definition 6 A PD is a positive finite measure $\mu_D = \sum_{p \in D} c_p \delta_p$, with δ_p being the Dirács delta centered in $p \in \mathbb{R}^2$, $D \subset \mathbb{R}_{x < y}^2$ being a finite set, and $c_p \in \mathbb{N}$. We refer to the set D as the support of the diagram.

Following Divol and Lacombe (2021) we give the following definition.

Definition 7 For any measure μ and for any subset $Z \subset \mathbb{R}^2$, we define:

$$\text{Pers}_Z(\mu) = \frac{1}{2} \int_Z (y - x) d\mu((x, y)).$$

When $Z = \mathbb{R}^2$, we simply write $\text{Pers}(\mu)$.

As proven in Skraba and Turner (2020), in the context of stability for linear operators defined on spaces of measures, we are forced to work with the 1-Wasserstein metric. To introduce such a metric with a notation convenient for the proofs that follow, we define the following terms.

Definition 8 Consider two diagrams μ_D and $\mu_{D'}$. A partial matching between $\mu_D = \sum_{p \in D} a_p \delta_p$ and $\mu_{D'} = \sum_{p \in D'} b_p \delta_p$ is a triplet $(D_\gamma, D'_\gamma, \gamma : D_\gamma \rightarrow D'_\gamma)$ such that:

- $D_\gamma \subset D$ and $D'_\gamma \subset D'$;
- $\gamma : D_\gamma \rightarrow D'_\gamma$ is a bijection.

We may indicate a partial matching just with γ , for the sake of brevity.

Given a partial matching γ between $\mu_D = \sum_{p \in D} a_p \delta_p$ and $\mu_{D'} = \sum_{p \in D'} b_p \delta_p$, for every $p \in D_\gamma$, we set $\gamma_p := \min\{a_p, b_{\gamma(p)}\}$. Similarly, for every $q \in D'_\gamma$, we set $\gamma_q := \min\{b_q, a_{\gamma^{-1}(q)}\}$. The cost of γ can then be defined as follows:

$$\begin{aligned} c(\gamma) := & \sum_{p \in D_\gamma} \gamma_p \|p - \gamma(p)\|_\infty + \sum_{p \in D_\gamma} (a_p - \gamma_p) \|p - \Delta\|_\infty + \sum_{q \in D'_\gamma} (b_q - \gamma_q) \|q - \Delta\|_\infty + \\ & \sum_{p \in D \setminus D_\gamma} a_p \|p - \Delta\|_\infty + \sum_{q \in D' \setminus D'_\gamma} b_q \|q - \Delta\|_\infty. \end{aligned} \tag{1}$$

Definition 9 The 1-Wasserstein distance between PDs is defined as:

$$W_1(\mu_D, \mu_{D'}) = \inf\{c(\gamma) \mid \gamma \text{ partial matching between } \mu_D \text{ and } \mu_{D'}\}.$$

Remark 1 The definition of the 1-Wasserstein distance adopted here is equivalent to other formulations in the literature. In particular, the bijection $\gamma : D_\gamma \rightarrow D'_\gamma$ can be interpreted as a transport map between the measures $\sum_{p \in D_\gamma} \gamma_p \delta_p$ and $\sum_{q \in D'_\gamma} \gamma_q \delta_q$, while the associated cost $c(\gamma)$ corresponds to the transportation cost, including the cost of sending the remaining mass of both diagrams to the diagonal Δ (see Divol and Lacombe (2021)).

We recall the following key result from Divol and Lacombe (2021).

Theorem 1

$$W_1(\mu_D, \mu_{D_n}) \rightarrow 0 \text{ if, and only if, } \mu_{D_n} \xrightarrow{v} \mu_D \text{ and } \text{Pers}(\mu_{D_n}) \rightarrow \text{Pers}(\mu_D).$$

2.4 Lift Zonoids of Discrete Measures

We now introduce the final components needed to define our topological summaries. Throughout, we adopt the following notation: for a point $p = (x, y) \in \mathbb{R}^2$, we set $(1, p) := (1, x, y) \in \mathbb{R}^3$.

As a preliminary step, we recall the construction of the lift zonoid associated with an integrable measure, as presented in Koshevoy and Mosler (1998); Hendrych and Nagy (2022). For simplicity and coherence with our setting, we restrict attention to discrete measures.

Definition 10 *Given a discrete measure $\mu = \sum_{i=1}^n c_i \delta_{p_i}$, $p_i \in \mathbb{R}^2$ and $c_i > 0$, the lift zonoid of μ is the following convex set (zonotope):*

$$Z_\mu = \bigoplus_{i=1}^n c_i [0, (1, p_i)] \subset \mathbb{R}^3,$$

with $[0, (1, p_i)]$ being the segment joining the origin $0 \in \mathbb{R}^3$ and the point $(1, p_i)$.

Note that the lift zonoid construction is linear: $\lambda_1 \mu_1 + \lambda_2 \mu_2 \mapsto \lambda_1 Z_{\mu_1} \oplus \lambda_2 Z_{\mu_2}$. Koshevoy and Mosler (1998); Hendrych and Nagy (2022) prove the following result.

Proposition 2 *Given an integrable measure μ and a sequence of integrable measures $\{\mu_n\}_{n \in \mathbb{N}}$, the following hold:*

$$d_H(Z_\mu, Z_{\mu_n}) \rightarrow 0 \text{ if, and only if, } \mu_n \xrightarrow{w} \mu \text{ and } \{\mu_n\}_{n \in \mathbb{N}} \text{ is uniformly integrable.}$$

3. Persistence Spheres

Now we finally introduce persistence spheres as the support functions (see Definition 2) of lift zonoids of (weighted) PDs, restricted to \mathbb{S}^2 .

As for other functional representations of PDs, see Adams et al. (2017), we need to re-weight diagrams with a function $\omega : \mathbb{R}^2 \rightarrow (0, 1]$ so that the weight assigned to points goes to zero as we approach Δ . Given a diagram $\mu_D = \sum_{p \in D} c_p \delta_p$ and a function $\omega : \mathbb{R}^2 \rightarrow (0, 1]$, we set $\mu_D^\omega := \sum_{p \in D} \omega(p) c_p \delta_p$.

Definition 11 *Given a PD μ_D and a function $\omega : \mathbb{R}^2 \rightarrow (0, 1]$, the persistence sphere (PS) of μ_D with weighting ω is defined as $\varphi_{\mu_D}^\omega := (h_{Z_{\mu_D^\omega}})_{|\mathbb{S}^2}$.*

For any function $\omega : \mathbb{R}^2 \rightarrow (0, 1]$ we set $\Gamma_\omega(p) := \omega(p)(1, p)$. We want to control the decay of ω as points approach the diagonal. We do so with the following technical conditions.

Definition 12 *A function $\omega : \mathbb{R}^2 \rightarrow (0, 1]$ is called a stable lift weighting if:*

- Γ_ω is C -Lipschitz for some $C > 0$;
- the following inequality is satisfied for every $p = (x, y) \in \mathbb{R}_{x < y}^2$ and some fixed $C' > 0$:

$$\| \Gamma_\omega(p) \|_2 \leq C' \left(\frac{y - x}{2} \right) = C' \| p - \Delta \|_\infty.$$

In Definition 12, we used the term “lift weighting” to emphasize its role in the context of lift zonoids. Since no ambiguity arises in this work, we will omit the qualifier “lift” from now on for brevity.

Definition 13 *A function $\omega : \mathbb{R}^2 \rightarrow (0, 1]$ is called an effective (lift) weighting if for any sequence of diagrams $\{\mu_{D_n}\}_{n \in \mathbb{N}}$:*

$$\lim_{r \rightarrow \infty} \sup_n \int_{B_r^c} \omega(p) \|p\|_2 d\mu_n(p) = 0 \implies \lim_{r \rightarrow \infty} \sup_n \text{Pers}_{B_r^c}(\mu_{D_n}) = 0.$$

Definition 13 controls the behavior of Γ_ω at infinity. To see that, note that, for every $\varepsilon > 0$, there is R such that for every $r > R$ we have: $\frac{\|p\|_2}{\|(1,p)\|_2} \geq 1 - \varepsilon$. For any such r :

$$(1 - \varepsilon) \sup_n \int_{B_r^c} \omega(p) \|(1,p)\|_2 d\mu_{D_n}(p) \leq \sup_n \int_{B_r^c} \omega(p) \|p\|_2 d\mu_{D_n}(p).$$

Which means that, in the context of the definition, we have:

$$\lim_{r \rightarrow \infty} \sup_n \int_{B_r^c} \|\Gamma_\omega(p)\|_2 d\mu_{D_n}(p) \rightarrow 0. \quad (2)$$

We now provide examples of stable and effective weightings.

Proposition 3 *Set $\lambda(p) := \frac{y-x}{2\|(1,p)\|_2}$. The following are stable weightings:*

$$\tilde{\omega}(p) = \lambda(p)^\alpha, \quad \omega_K(p) = \frac{2}{\pi} \arctan\left(\frac{\lambda(p)^\alpha}{K^\alpha}\right),$$

for any $K > 0$ and $\alpha \geq 1$. They are also effective weightings for $\alpha = 1$.

We conclude this section highlighting that, by linearity, the PS of a PD $\mu_D = \sum_{p \in D} c_p \delta_p$, with weighting function ω , can be explicitly written as:

$$\varphi_{\mu_D}^\omega(v) = h_{Z_{\mu_D^\omega}}(v) = \sum_{p \in D} \omega(p) c_p \text{ReLU}(\langle v, (1, p) \rangle), \quad \text{with } \text{ReLU}(x) := \max\{0, x\}. \quad (3)$$

3.1 Continuity Theorems

We now state our main results, which contain the continuity properties anticipated in the introduction. First we state and prove them in terms of lift zonoids and Hausdorff distances, which simplifies the proofs, and then, using Proposition 1, we derive the bi-continuity of PSs.

Theorem 2 *Let $\mu_D, \mu_{D'}$ be PDs and let $\omega : \mathbb{R}^2 \rightarrow \mathbb{R}$ be a stable weighting. We have:*

$$d_H(Z_{\mu_D^\omega}, Z_{\mu_{D'}^\omega}) \leq \max\{C, C'\} \cdot W_1(\mu_D, \mu_{D'}),$$

with $C, C' > 0$ being the stability constants of ω (see Definition 12).

Theorem 3 *Let $\{\mu_{D_n}\}_{n \in \mathbb{N}}$ be a sequence of PDs such that $d_H(Z_{\mu_{D_n}^\omega}, Z_{\mu_D^\omega}) \rightarrow 0$, with $\omega : \mathbb{R}^2 \rightarrow \mathbb{R}$ being an effective weighting. Then, $W_1(\mu_{D_n}, \mu_D) \rightarrow 0$.*

Summarizing the statements of Theorem 2 and Theorem 3, and writing them replacing lift zonoids with persistence spheres, we obtain the following result.

Corollary 1 *Within the setting of the previous results, we have:*

- for every $p \in [1, \infty]$ there exist $C_p > 0$ such that, for every pair of diagrams $\mu_D, \mu_{D'}$, we have $\|\varphi_{\mu_D}^\omega - \varphi_{\mu_{D'}}^\omega\|_p \leq C_p W_1(\mu_D, \mu_{D'})$;
- if $\|\varphi_{\mu_D}^\omega - \varphi_{\mu_{D_n}}^\omega\|_\infty \rightarrow 0$, then $W_1(\mu_{D_n}, \mu_D) \rightarrow 0$.

Remark 2 *Gotovac Dogaš and Mandarić (2025) define their functional representation as $\varphi_{\mu_D}^\omega$, with $\omega(p) = y - x$. This weighting is not stable, since for any $C > 0$,*

$$\|\Gamma_\omega(p)\| > C\|p - \Delta\|_\infty, \quad (4)$$

whenever $\|p\|_2$ is sufficiently large. In particular, the map $\mu_D \mapsto \varphi_{\mu_D}^\omega$ fails to be stable. For instance, let $D_n = \{p_n\} = \{(n^2, n^2 + \frac{1}{n})\}$. Then $Z_{D_n}^\omega = \frac{1}{n}[0, (1, p_n)]$. If $D = \emptyset$, we obtain

$$W_1(D_n, D) = \frac{1}{n} \xrightarrow{n \rightarrow \infty} 0, \quad d_H(Z_D, Z_{D_n}) \geq \frac{\sqrt{2}}{n} n^2 \xrightarrow{n \rightarrow \infty} \infty.$$

On the other hand, by Equation (4) one can verify that $\omega(p) = y - x$ is effective. Consequently, Theorem 3 holds for the functional representation in Gotovac Dogaš and Mandarić (2025), although this fact is not established in that work.

4. Experiments

We evaluated PSs on a range of regression and classification case studies, comparing their performance with persistence images (PIs), persistence landscapes (PLs), and the sliced Wasserstein kernel (SWK). For PSs, PIs, and PLs, we employed both support vector machines (SVM) with radial-basis kernels (denoted “-SVM” in Table 1) and penalized linear/logistic regressions (denoted “-Reg” in Table 1). Performance was assessed using R^2 for regression tasks and accuracy for classification tasks, averaged over 10 independent runs. See also Figure 1.

4.1 Datasets

We now briefly describe the case studies under consideration, organizing them according to the source of the datasets. Our selection draws from a diverse range of origins: some datasets were generated by us, others stem from benchmark case studies in functional data analysis (FDA) and shape analysis, and additional ones were taken from publications where PDs were publicly available—allowing us to bypass a full pipeline implementation. In making these choices, we also prioritized diversity in the underlying data types, including functions, time series, 3D meshes, graphs, and point clouds.

“Eyeglasses” Case Study The “Eyeglasses” dataset is a regression case study we designed using the *eyeglasses* generative model from the `scikit-tda` python package (Saul and Tralie, 2019). This model takes two radii as parameters, and a noise variable which was kept equal to 1. The first radius was always set equal to 20, while the second was sampled according to a normal distribution with mean 10 and standard variation 2.5. We sampled 2000 point clouds and used a 30% – 70% split between training and test data; threefold cross-validation was used to select hyper-parameters, and 1-dimensional PDs were obtained from the Vietoris-Rips filtration.

Functional datasets from the `scikit-fda` Package For the following functional datasets, we used zero-dimensional persistent homology derived from the sublevel set filtration. Data were split into training and test sets in a 70%–30% ratio, and hyperparameters were selected via threefold cross-validation. All datasets are freely available in the `scikit-fda` Python package (Ramos-Carreño et al., 2024).

The “Tecator” dataset (<https://lib.stat.cmu.edu/datasets/tecator>) consists of publicly available measurements collected using the “Tecator Infratec Food and Feed Analyzer”. Building on the derivatives of these curves, we explore the same regression problem as in Ferraty and Vieu (2006), trying to regress the fat content of the food samples.

The “NO_x” dataset (Febrero et al., 2008) contains hourly measurements of daily nitrogen oxides (NO_x) emissions in the Barcelona area. The data is labeled based on whether the emission curve was recorded on a weekday or a weekend, and our goal is thus to reconstruct this labeling through supervised classification.

The “Growth” dataset (Tuddenham and Snyder, 1954), also known as “The Berkeley Growth Study”, contains height measurements of girls and boys, recorded yearly between ages 1 and 18. A common approach is to analyze the first derivative of the growth curves to distinguish growth dynamics between boys and girls (Vitelli et al., 2010).

Datasets from Bandiziol and De Marchi (2024) The classification case studies involving the datasets “DYN SYS”, “ENZYMES JACC”, “POWER”, and “SHREC14” were taken from Bandiziol and De Marchi (2024). As in the previous setting, we used a 70%–30% train–test split, with hyperparameters selected via threefold cross-validation. For these datasets, we could directly rely on the PDs associated with the classification tasks, which are publicly available at https://github.com/cinziabandiziol/persistence_kernels.

In selecting the problems, we prioritized classification tasks with balanced classes and diversity in data type, including point clouds, graphs, time series, and 3D meshes. We now summarize the considered datasets; further details can be found in Bandiziol and De Marchi (2024).

The dataset “DYN SYS”, first introduced in Adams et al. (2017) and referred to as “Orbit Recognition” in Bandiziol and De Marchi (2024), consists of point clouds generated by a one-parameter discrete dynamical system, with the parameter ranging in {2.5, 3.5, 4, 4.1, 4.3}. The classification task, considered in Adams et al. (2017); Bandiziol and De Marchi (2024) as well as in our work, is to predict the parameter value from the associated point cloud, a problem also studied in Carriere et al. (2017). For each parameter value, 50 independent point clouds were generated, each containing 1000 points with starting positions chosen uniformly at random, yielding a dataset of 250 elements. The PDs computed by Bandiziol and De Marchi (2024) contain only one-dimensional features.

The dataset “ENZYMES JACC” addresses a graph classification problem. Graphs represent protein tertiary structures obtained from the BRENDA enzyme database (<https://www.brenda-enzymes.org/>), and the task is to classify each of the 600 graphs into one of six enzyme classes. Edges were weighted by their Jaccard index, and PDs were computed from the resulting sublevel set filtration, combining both zero- and one-dimensional features.

The dataset “POWER”, from the UCR Time Series Classification Archive (https://www.cs.ucr.edu/~eamonn/time_series_data_2018/), consists of 1096 time series. The pipeline in this case applied the sliding window embedding (Ravishanker and Chen, 2021), followed by the extraction of zero-, one-, and two-dimensional features, which were then merged into a single diagram for each time series.

Finally, the dataset “SHREC14” (Pickup et al., 2014) is a benchmark for non-rigid 3D shape classification. It contains meshes of human models across 20 poses and 15 body

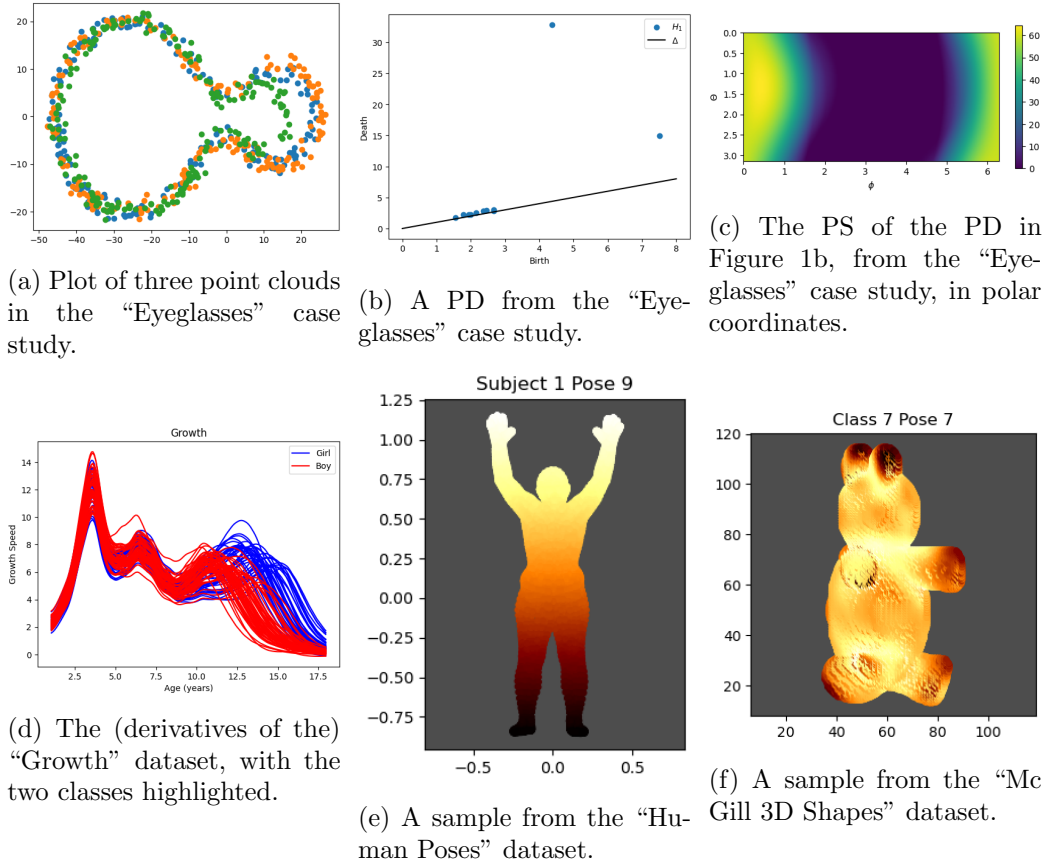


Figure 1: Data, PDs, and PSs from some of the experiments in Section 4.

types (e.g., man, woman, child), resulting in 300 total meshes. In Bandiziol and De Marchi (2024), the Heat Kernel Signature (HKS) (Sun et al., 2009; Bronstein and Kokkinos, 2010) was used to extract one-dimensional PDs from the corresponding sublevel set filtrations.

Datasets “Human Poses” and “Mc Gill 3D Shapes” The remaining datasets, “Human Poses” and “McGill 3D Shapes”, were obtained from <https://github.com/ctralie/TDALabs/blob/master/3DShapes.ipynb>. The corresponding classification pipelines are documented in the referenced notebook: for the human pose task, a sublevel set filtration of the height function was used, while for the McGill shape classification task, a sublevel set filtration of the HKS was applied. We note that the “McGill 3D Shapes” dataset used here is a subsample of the original version, which is no longer fully accessible online. In both case studies, the train–test split (80%–20%) was imposed by the dataset limitation of having only 10 samples per class.

4.2 Implementation Details

As already mentioned, we considered two types of pipelines based on the chosen vectorization method: SVM and penalized linear/logistic regression. Both were implemented using the `scikit-learn` Python package (Pedregosa et al., 2011). For regression and classification with linear/logistic models, we employed ℓ_2 regularization to mitigate overfitting.

Regression and SVM Parameters First we consider hyperparameters associated with the learning models (“-SVM” vs. “-Reg”).

- “-SVM”: all SVM pipelines required a regularization parameter C , chosen from $\{0.001, 0.01, 0.1, 1, 10, 100, 1000, 10000\}$. Except for SWK, where the kernel was pre-computed, all other methods used the radial basis function kernel.
- “-Reg”: for Ridge regression, the penalization parameter α was chosen from $\{0.000001, 0.00001, 0.0001\}$ while for penalized logistic regression the C parameter was selected from $\{1, 10, 100, 1000, 10000\}$.

Linearization Methods Parameters Now we consider hyperparameters tied to each linearization method.

- PS: we employed the weighting function ω_K^α defined in the main text, with $\alpha = 1$, and exploring $K \in \{0.00001, 0.0001, 0.001, 0.01, 0.1, 0.2, 0.3, 0.4, 0.5\}$. Since PS are functions on \mathbb{S}^2 expressed in spherical coordinates, we projected them onto a spline basis and applied functional principal component analysis (FPCA) on the sphere—retaining all components—to obtain an orthonormal representation suitable for penalized models in `scikit-learn`. FPCA was implemented using the Rayleigh quotient approach, which accommodates non-orthonormal bases. We used a grid of size 200×100 to evaluate PSs, and a spherical spline basis with 561 elements for the FPCA.
- PI: using the `scikit-tda persim` module, we selected the *pixel_size* by enclosing all PDs in a rectangle (expressed in birth–persistence coordinates) and dividing its shortest side by n' , with $n' \in \{100, 500\}$, rounding to the nearest power of 10 for numerical stability. We used the default bivariate Gaussian kernel, with $\sigma = \text{pixel_size}/m$, where $m \in \{1, 10, 100\}$. The exponent n in the *weight_params* dictionary (corresponding to persistence weighting) was varied in $\{1, 2, 4, 8\}$.
- PL: for landscapes, we considered the first five landscapes evaluated on a fixed common grid across the dataset, and we concatenated them. No hyperparameters needed tuning.
- SWK: we used the implementation of the sliced Wasserstein kernel in the `gudhi` library (Project, 2025), fixing $M = 100$ and exploring the scaling parameter $\sigma \in \{0.00001, 0.0001, 0.001, 0.01, 0.1, 1, 10\}$ for the Gram matrix.

Computational Aspects The computation of a PS scales linearly with both the number of points in the diagram and the size of the evaluation grid. As shown in Equation (3), it reduces to evaluating standard mathematical functions in one or two variables. Since these evaluations are independent across points, the process can be efficiently parallelized with $O(1)$ work per core. As a result, PSs are potentially cheaper than PIs, which require binning and integration, and PLs, whose fastest known algorithm has complexity $O(n \log n + nN)$ (Bubenik and Dłotko, 2017), where $n = \#D$ and N is the number of nonzero landscapes. Approximating SWK incurs a similar computational cost of $O(n \log n)$ (Carriere et al., 2017). When evaluated on a grid, PSs have the same dimensionality as PIs on a comparable grid, since both are scalar fields on 2D manifolds.

Working with scalar fields on the sphere poses challenges for standard norm-penalized statistical methods (e.g., Ridge regression), which typically assume either a uniform grid or an orthonormal basis projection. To address this, we represented each PS using a spline basis and applied functional FPCA to obtain an orthonormal representation. While this approach increased computational cost, runtimes remained manageable in our experiments. For substantially larger datasets in combination with penalized methods, tailored implementations could further improve efficiency.

	PSph-SVM	PSph-Lin	PI-SVM	PI-Lin	PL-SVM	PL-Lin	SWK
Regression							
Regression Case Study	0.967	0.976	0.672	0.769	0.964	0.883	0.960
Tecator	0.962 (0.004)	0.960 (0.007)	0.928 (0.029)	0.922 (0.018)	0.939 (0.016)	0.837 (0.048)	0.953 (0.010)
Classification							
Growth	0.871 (0.064)	0.889 (0.045)	0.525 (0.095)	0.536 (0.086)	0.782 (0.051)	0.767 (0.107)	0.768 (0.058)
NOx	0.877 (0.034)	0.826 (0.035)	0.803 (0.073)	0.563 (0.102)	0.794 (0.047)	0.751 (0.040)	0.840 (0.055)
DYN_SYS	0.809 (0.040)	0.797 (0.030)	0.709 (0.020)	0.819 (0.017)	0.849 (0.029)	0.823 (0.027)	0.828 (0.028)
ENZYMES_JACC	0.288 (0.064)	0.278 (0.036)	-	-	0.236 (0.026)	0.254 (0.028)	0.283 (0.055)
POWER	0.761 (0.017)	0.738 (0.021)	0.682 (0.026)	0.700 (0.020)	0.746 (0.014)	0.719 (0.030)	0.767 (0.15)
SHREC14	0.885 (0.057)	0.926 (0.019)	0.905 (0.029)	0.897 (0.024)	0.914 (0.021)	0.931 (0.013)	0.886 (0.092)
Human Poses	0.580 (0.081)	0.600 (0.084)	0.407 (0.144)	0.503 (0.046)	0.460 (0.118)	0.480 (0.105)	0.345 (0.082)
McGill 3D Shapes	0.383 (0.094)	0.489 (0.173)	0.678 (0.060)	0.045 (0.052)	0.650 (0.093)	0.511 (0.150)	0.567 (0.13)

Table 1: Results of the case studies: we report average R^2 for regression and average accuracy for classification, across 10 independent repetitions. Between brackets we reported the standard deviation of the scores. Best performing pipelines are reported in bold.

Finally, as with PIs, modifying the weighting function ω requires recomputing the entire persistence sphere. This differs from SWK, where the Gram matrix remains fixed across different values of σ .

4.3 Results

As shown in Table 1, persistence spheres consistently matched or surpassed established topological representations—persistence images, persistence landscapes, and the sliced Wasserstein kernel—across regression and classification tasks spanning functional data, time series, graphs, meshes, and point clouds. The main exception was the McGill 3D Shapes dataset, where PIs and PLs performed better, possibly due the high variability induced by the limited number of samples per class.

5. Conclusion and Broader Impact

We introduced persistence spheres, a novel functional representation of persistence diagrams that is both Lipschitz continuous and admits a continuous inverse on its image, yielding a bi-continuous correspondence with respect to the 1-Wasserstein geometry. This combination of stability and geometric fidelity sets persistence spheres apart from existing vectorization methods. By providing a representation that is scalable, robust, and geometrically faithful, persistence spheres enable a more principled integration of topological information into machine learning pipelines. Empirically, we find that persistence spheres are not only competitive with, but frequently outperform, widely used alternatives such as persistence images, persistence landscapes, and sliced Wasserstein kernels.

Several avenues for future work remain. Alternative weighting schemes may yield more expressive summaries. Tools from functional data analysis could support advanced statistical methodologies, such as confidence sets, hypothesis testing, and limit theorems for point processes. Reconstruction techniques for recovering PDs from scalar fields on the sphere are under development. Visualization strategies could enhance interpretability. Integration, via differentiable loss functions, with modern representation learning techniques may broaden applicability. Finally, extending the construction to signed measures could provide a natural vectorization for bi-parameter persistence.

In summary, persistence spheres advance the state of topological machine learning by offering a theoretically rigorous, practically effective, and extensible framework for embedding topological information into learning systems.

Reproducibility Statement

Section 4.2 provides the main details required to reproduce our results. All datasets used are publicly available, and the explicit formulation of our method in Section 3 ensures reproducibility.

The Use of Large Language Models

Large Language Models were occasionally employed to refine and polish the writing.

Acknowledgments

We thank C. A. N. Biscio, N. Chenavier, and N. R. Franco for the very helpful discussions.

Code

The code employed to generate the results presented in this work has not yet been publicly released. We intend to make it available in the near future; in the meantime, it can be obtained upon request

References

Henry Adams, Tegan Emerson, Michael Kirby, Rachel Neville, Chris Peterson, Patrick Shipman, Sofya Chepushtanova, Eric Hanson, Francis Motta, and Lori Ziegelmeier. Persistence images: A stable vector representation of persistent homology. *Journal of Machine Learning Research*, 18(8):1–35, 2017.

Dashti Ali, Aras Asaad, Maria-Jose Jimenez, Vidit Nanda, Eduardo Paluzo-Hidalgo, and Manuel Soriano-Trigueros. A survey of vectorization methods in topological data analysis. *IEEE Transactions on Pattern Analysis and Machine Intelligence*, 45(12):14069–14080, 2023.

Aras Asaad, Dashti Ali, Taban Majeed, and Rasber Rashid. Persistent homology for breast tumor classification using mammogram scans. *Mathematics*, 10(21):4039, 2022.

Cinzia Bandiziol and Stefano De Marchi. Persistence symmetric kernels for classification: A comparative study. *Symmetry*, 16(9):1236, 2024.

Christophe AN Biscio and Jesper Møller. The accumulated persistence function, a new useful functional summary statistic for topological data analysis, with a view to brain artery trees and spatial point process applications. *Journal of Computational and Graphical Statistics*, 28(3):671–681, 2019.

Michael M Bronstein and Iasonas Kokkinos. Scale-invariant heat kernel signatures for non-rigid shape recognition. In *2010 IEEE computer society conference on computer vision and pattern recognition*, pages 1704–1711. IEEE, 2010.

Peter Bubenik. Statistical topological data analysis using persistence landscapes. *Journal of Machine Learning Research*, 16:77–102, 2015.

Peter Bubenik and Paweł Dłotko. A persistence landscapes toolbox for topological statistics. *Journal of Symbolic Computation*, 78:91–114, 2017.

Mathieu Carrière and Ulrich Bauer. On the metric distortion of embedding persistence diagrams into separable hilbert spaces. In *35th International Symposium on Computational Geometry (SoCG 2019)*, pages 21–1. Schloss Dagstuhl–Leibniz-Zentrum für Informatik, 2019.

Mathieu Carriere, Marco Cuturi, and Steve Oudot. Sliced wasserstein kernel for persistence diagrams. In *International conference on machine learning*, pages 664–673. PMLR, 2017.

Barbara Di Fabio and Massimo Ferri. Comparing persistence diagrams through complex vectors. In *International conference on image analysis and processing*, pages 294–305. Springer, 2015.

Vincent Divol and Théo Lacombe. Understanding the topology and the geometry of the space of persistence diagrams via optimal partial transport. *Journal of Applied and Computational Topology*, 5:1–53, 2021.

Herbert Edelsbrunner and John L Harer. *Computational topology: an introduction*. American Mathematical Society, 2010.

Manuel Febrero, Pedro Galeano, and Wenceslao González-Manteiga. Outlier detection in functional data by depth measures, with application to identify abnormal nox levels. *Environmetrics*, 19(4):331–345, 2008.

Frédéric Ferraty and Philippe Vieu. *Nonparametric functional data analysis: theory and practice*. Springer Verlag, NY, 2006. URL <https://doi.org/10.1007/0-387-36620-2>.

Vesna Gotovac Dogaš and Marcela Mandarić. Topological data analysis for random sets and its application in detecting outliers and goodness of fit testing. *Statistical Methods & Applications*, pages 1–45, 2025.

František Hendrych and Stanislav Nagy. A note on the convergence of lift zonoids of measures. *Stat*, 11(1):e453, 2022.

Sara Kališnik. Tropical coordinates on the space of persistence barcodes. *Foundations of Computational Mathematics*, 19(1):101–129, 2019.

Olav Kallenberg. *Foundations of modern probability*. Springer, 1997.

Gleb Koshevoy and Karl Mosler. Lift zonoids, random convex hulls and the variability of random vectors. 1998.

Genki Kusano, Kenji Fukumizu, and Yasuaki Hiraoka. Kernel method for persistence diagrams via kernel embedding and weight factor. *Journal of Machine Learning Research*, 18(189):1–41, 2018.

Yuriy Mileyko, Sayan Mukherjee, and John Harer. Probability measures on the space of persistence diagrams. *Inverse Problems*, 27(12):124007, 2011.

Atish Mitra and Ziga Virk. Geometric embeddings of spaces of persistence diagrams with explicit distortions. *arXiv preprint arXiv:2401.05298*, 2024.

Anthea Monod, Sara Kalisnik, Juan Ángel Patino-Galindo, and Lorin Crawford. Tropical sufficient statistics for persistent homology. *SIAM Journal on Applied Algebra and Geometry*, 3(2):337–371, 2019.

Michael Moor, Max Horn, Bastian Rieck, and Karsten Borgwardt. Topological autoencoders. In *International conference on machine learning*, pages 7045–7054. PMLR, 2020.

Steve Y Oudot. *Persistence theory: from quiver representations to data analysis*, volume 209. American Mathematical Society Providence, 2015.

Theodore Papamarkou, Tolga Birdal, Michael M Bronstein, Gunnar E Carlsson, Justin Curry, Yue Gao, Mustafa Hajij, Roland Kwitt, Pietro Lio, Paolo Di Lorenzo, et al. Position: Topological deep learning is the new frontier for relational learning. In *International Conference on Machine Learning*, pages 39529–39555. PMLR, 2024.

F. Pedregosa, G. Varoquaux, A. Gramfort, V. Michel, B. Thirion, O. Grisel, M. Blondel, P. Prettenhofer, R. Weiss, V. Dubourg, J. Vanderplas, A. Passos, D. Cournapeau, M. Brucher, M. Perrot, and E. Duchesnay. Scikit-learn: Machine learning in Python. *Journal of Machine Learning Research*, 12:2825–2830, 2011.

D. Pickup, X. Sun, P. L. Rosin, R. R. Martin, Z. Cheng, Z. Lian, M. Aono, A. Ben Hamza, A. Bronstein, M. Bronstein, S. Bu, U. Castellani, S. Cheng, V. Garro, A. Giachetti, A. Godil, J. Han, H. Johan, L. Lai, B. Li, C. Li, H. Li, R. Litman, X. Liu, Z. Liu, Y. Lu, A. Tatsuma, and J. Ye. SHREC’14 track: Shape retrieval of non-rigid 3d human models. In *Proceedings of the 7th Eurographics workshop on 3D Object Retrieval*, EG 3DOR’14. Eurographics Association, 2014.

The GUDHI Project. *GUDHI User and Reference Manual*. GUDHI Editorial Board, 3.11.0 edition, 2025. URL <https://gudhi.inria.fr/doc/3.11.0/>.

Chi Seng Pun, Si Xian Lee, and Kelin Xia. Persistent-homology-based machine learning: a survey and a comparative study. *Artificial Intelligence Review*, 55(7):5169–5213, 2022.

Carlos Ramos-Carreño, José L. Torrecilla, Miguel Carbajo Berrocal, Pablo Marcos Manchón, and Alberto Suárez. scikit-fda: A Python Package for Functional Data Analysis. *Journal of Statistical Software*, 109(2):1–37, May 2024.

Nalini Ravishanker and Renjie Chen. An introduction to persistent homology for time series. *Wiley Interdisciplinary Reviews: Computational Statistics*, 13(3):e1548, 2021.

Jan Reininghaus, Stefan Huber, Ulrich Bauer, and Roland Kwitt. A stable multi-scale kernel for topological machine learning. In *Proceedings of the IEEE conference on computer vision and pattern recognition*, pages 4741–4748, 2015.

R Tyrrell Rockafellar. *Convex Analysis*, volume 28. Princeton University Press, 1997.

Gabriella Salinetti and Roger J.-B. Wets. On the convergence of sequences of convex sets in finite dimensions. *SIAM Review*, 21(1):18–33, 1979.

Nathaniel Saul and Chris Tralie. Scikit-tda: Topological data analysis for python, 2019. URL <https://doi.org/10.5281/zenodo.2533369>.

Primoz Skraba and Katharine Turner. Wasserstein stability for persistence diagrams. *arXiv preprint arXiv:2006.16824*, 2020.

Jian Sun, Maks Ovsjanikov, and Leonidas Guibas. A concise and provably informative multi-scale signature based on heat diffusion. In *Computer graphics forum*, volume 28, pages 1383–1392. Wiley Online Library, 2009.

RD Tuddenham and MM Snyder. Physical growth of california boys and girlsfrom birth to age 18. *Calif. Publ. Child Develop*, 1:183–364, 1954.

Valeria Vitelli, Laura Maria Sangalli, Piercesare Secchi, and Simone Vantini. Functional clustering and alignment methods with applications. *Communications in Applied and Industrial Mathematics*, 1(1):205–224, 2010. URL <https://doi.org/10.1685/2010CAIM486>.

Jeremy Wayland, Corinna Coupette, and Bastian Rieck. Mapping the multiverse of latent representations. In *International Conference on Machine Learning*. PMLR, 2024.

Appendix A. Additional Implementation Details

We conclude with a note on our current cross-validation pipeline for PSs. The code is designed to flexibly explore a wide parameter space (e.g., varying α rather than fixing $\alpha = 1$), but this comes at the cost of some redundant computations. Specifically, for each PD, we project the PS of every individual point in the diagram onto a spline basis (without applying a weighting function). This design allows us to later change the weighting function ω and, by linearity, reuse the existing projections without repeating the spline projection step. While this is less efficient than projecting the entire PS directly, the latter approach would require reprojecting whenever ω changes. Striking the right balance between these two strategies, depending on the size of the parameter space, could lead to further efficiency improvements.

Appendix B. Proofs of the Results

Proposition 4 Set $\lambda(p) := \frac{y-x}{2\|(1,p)\|_2}$. The following are stable weightings:

$$\tilde{\omega}(p) = \lambda(p)^\alpha, \quad \omega_K(p) = \frac{2}{\pi} \arctan\left(\frac{\lambda(p)^\alpha}{K^\alpha}\right),$$

for any $K > 0$ and $\alpha \geq 1$. They are also effective weightings for $\alpha = 1$.

Proof

The functions Γ_ω have the following forms:

$$\begin{aligned} \Gamma_{\tilde{\omega}}(x, y) &= \frac{(y-x)^\alpha}{2^\alpha \|(1, x, y)\|_2^\alpha} (1, x, y); \\ \Gamma_{\omega_k}(x, y) &= \frac{2}{\pi} \arctan\left(\frac{(y-x)^\alpha}{2^\alpha K^\alpha \|(1, x, y)\|_2^\alpha}\right) (1, x, y). \end{aligned}$$

Lipschitzianity is obtained because the components of the functions $\Gamma_{\tilde{\omega}}$ and Γ_{ω_K} are differentiable and have bounded partial derivatives on $\mathbb{R}_{x < y}^2$.

To check the norm condition for stability, we write down the expressions of $\|\Gamma_\omega\|_2$:

$$\begin{aligned} \|\Gamma_{\tilde{\omega}}(x, y)\|_2 &= \frac{(y-x)^\alpha}{2^\alpha \|(1, x, y)\|_2^{\alpha-1}}; \\ \|\Gamma_{\omega_k}(x, y)\|_2 &= \frac{2}{\pi} \arctan\left(\frac{(y-x)^\alpha}{2^\alpha K^\alpha \|(1, x, y)\|_2^\alpha}\right) \|(1, x, y)\|_2. \end{aligned}$$

At this point, we observe that:

$$\frac{(y-x)^{\alpha-1}}{2^{\alpha-1} \|(1, x, y)\|_2^{\alpha-1}} \in [0, 1];$$

and that:

$$\arctan\left(\frac{(y-x)^\alpha}{2^\alpha K^\alpha \|(1, x, y)\|_2^\alpha}\right) \|(1, x, y)\|_2 \leq \frac{(y-x)^\alpha}{2^\alpha K^\alpha \|(1, x, y)\|_2^{\alpha-1}}.$$

The first observation is enough to prove stability for $\tilde{\omega}$, while the second and the first observations, combined, prove it for ω_K .

Now we prove that both weightings are effective for $\alpha = 1$, exploiting Equation (2). Note that the functions have become:

$$\begin{aligned} \|\Gamma_{\tilde{\omega}}(x, y)\|_2 &= \frac{(y-x)}{2} = \|p - \Delta\|_\infty; \\ \|\Gamma_{\omega_K}(x, y)\|_2 &= \frac{2}{\pi} \arctan\left(\frac{(y-x)}{2K \|(1, x, y)\|_2}\right) \|(1, x, y)\|_2. \end{aligned}$$

To see that $\Gamma_{\tilde{\omega}}$ is effective, it suffices to observe that, plugging the expression of $\|\Gamma_{\tilde{\omega}}\|_2$ in Equation (2), we directly obtain the thesis.

Now we deal with Γ_{ω_K} . Set $\mu_{D_n} = \sum_{p \in D_n} a_{n,p} \delta_p$.

We rewrite Equation (2) as:

$$\lim_{r \rightarrow \infty} \sup_n \sum_{p \in D_n, \|p\|_2 > r} \|\Gamma_{\omega_K}(p)\|_2 \leq \lim_{r \rightarrow \infty} \sup_n \sum_{p \in D_n, \|p\|_2 > r} a_{n,p} \|\Gamma_{\omega_K}(p)\|_2 \rightarrow 0.$$

Thus, for every $\varepsilon > 0$, there is $R > 0$ such that, for every $r > R$ the following holds:

$$\sup_n \sum_{p \in D_n, \|p\|_2 > r} \|\Gamma_{\omega_K}(p)\|_2 < \varepsilon. \quad (5)$$

Hence, for every n , we have:

$$\sum_{p=(x,y) \in D_n, \|p\|_2 > r} \arctan\left(\frac{(y-x)}{2K \|(1, x, y)\|_2}\right) < \frac{\pi \varepsilon}{2r}. \quad (6)$$

In particular, Equation (6) implies $\frac{(y-x)}{2K \|(1, x, y)\|_2} \rightarrow 0$ for $r \rightarrow \infty$. Equivalently, for every $C > 0$, there is r_C such that $\frac{(y-x)}{2K \|(1, x, y)\|_2} < C$.

The key observation now, is that, due to the concavity of $z \mapsto \arctan(z)$, which is easy to see due to the strict monotonicity of its derivative $\frac{1}{1+z^2}$, we have:

$$\frac{\arctan(\varepsilon)}{\varepsilon} z \leq \arctan(z) \leq z$$

for every $z \in [0, \varepsilon]$, and every fixed $\varepsilon \geq 0$. In fact, $z \mapsto \frac{\arctan(\varepsilon)}{\varepsilon} z$ is the straight line joining $(0, 0)$ and $(\varepsilon, \arctan(\varepsilon))$. Thus, for every $C > 0$ and for every r_C such that $\frac{(y-x)}{2K \|(1, x, y)\|_2} < C$, we have for every n :

$$C' \sum_{p \in D_n, \|p\|_2 > r_C} \frac{a_{n,p}(y-x)}{2} \leq \sum_{p \in D_n, \|p\|_2 > r_C} \frac{2a_{n,p}}{\pi} \arctan\left(\frac{(y-x)}{2K \|(1, x, y)\|_2}\right) \|(1, x, y)\|_2,$$

with $C' = \frac{2 \arctan(C)}{\pi C K}$.

In particular, we can find $C' > 0$ such that:

$$C' \lim_{r \rightarrow \infty} \sup_n \text{Pers}(\mu_{D_n}) \leq \lim_{r \rightarrow \infty} \sup_n \sum_{p \in D_n, \|p\|_2 > r} a_{n,p} \|\Gamma_{\omega_K}(p)\|_2 \rightarrow 0.$$

And the thesis follows. ■

Theorem 4 Let $\mu_D, \mu'_{D'}$ be PDs and let $\omega : \mathbb{R}^2 \rightarrow \mathbb{R}$ be a stable weighting. We have:

$$d_H(Z_{\mu_D^\omega}, Z_{\mu'_{D'}^\omega}) \leq \max\{C, C'\} W_1(\mu_D, \mu_{D'}),$$

with $C, C' > 0$ being the stability constants of ω .

Proof Consider $\mu_D = \sum_{p \in D} a_p \delta_p, \mu_{D'} = \sum_{q \in D'} b_q \delta_q$ and a partial matching γ between them. Without loss of generality, suppose $C = C'$.

A generic point in $Z_{\mu_D^\omega}$ has the form:

$$P = \sum_{p \in D} a_p s_p \Gamma_\omega(p) \in Z_{\mu_D^\omega},$$

with $s_p \in [0, 1]$. We start by considering $p \in D_\gamma$ and $P \in Z_{\mu_D^\omega}$ with the following form:

$$P = \gamma_p \Gamma_\omega(p). \quad (7)$$

Note that, by definition, $\gamma_p \in \mathbb{N}$ and $\gamma_p \geq 1$.

Consider the point:

$$Q = \gamma_p \Gamma_\omega(\gamma(p)).$$

Since $\gamma_p \leq b_{\gamma(p)}$, there is $s \in [0, 1]$ such that $s b_{\gamma(p)} = \gamma_p$. Thus, $Q \in Z_{\mu_{D'}^\omega}$.

We have:

$$\|P - Q\|_2 \leq \gamma_p \|\Gamma_\omega(p) - \Gamma_\omega(\gamma(p))\|_2 \leq \gamma_p C \|p - \gamma(p)\|_2^\alpha.$$

For P in the form of Equation (7), we define $\Phi(P) := Q$.

Consider now a generic $P \in Z_{\mu_D^\omega}$:

$$P = \sum_{p \in D} a_p s_p \Gamma_\omega(p) = \sum_{p \in D_\gamma} \gamma_p s_p \Gamma_\omega(p) + \sum_{p \in D_\gamma} (a_p - \gamma_p) s_p \Gamma_\omega(p) + \sum_{p \in D - D_\gamma} a_p s_p \Gamma_\omega(p),$$

We build Q as follows:

$$Q = \sum_{p \in D_\gamma} s_p \Phi(\gamma_p \Gamma_\omega(p)).$$

We have:

$$\begin{aligned} \|P - Q\|_2 &\leq \sum_{p \in D_\gamma} s_p \gamma_p \|\Gamma_\omega(p) - \Gamma_\omega(\gamma(p))\|_2 + \sum_{p \in D_\gamma} s_p (a_p - \gamma_p) \|\Gamma_\omega(p)\|_2 + \\ &\quad \sum_{p \in D - D_\gamma} s_p a_p \|\Gamma_\omega(p)\|_2. \end{aligned} \quad (8)$$

Plugging into Equation (8) the following facts:

1. $\|\Gamma_\omega(p)\|_2 \leq C \|p - \Delta\|_\infty;$
2. $\|\|\|_2 \leq \sqrt{2} \|\|_\infty;$
3. $s_p \leq 1$ for every $p \in D,$

we obtain:

$$\begin{aligned} & \|P - Q\|_2 \leq \\ & C \left(\sqrt{2} \sum_{p \in D_\gamma} \gamma_p \|p - \gamma(p)\|_\infty + \sum_{p \in D_\gamma} (a_p - \gamma_p) \|p - \Delta\|_\infty + \sum_{p \in D - D_\gamma} a_p \|p - \Delta\|_\infty \right). \end{aligned}$$

Since we can do this construction for any partial matching γ , for every $P \in Z_{\mu_D^\omega}$, we found Q such that:

$$\|P - Q\|_2 \leq CW_1(\mu_D, \mu_{D'}).$$

Reversing the role of μ_D and $\mu_{D'}$ we obtain the thesis. \blacksquare

Theorem 5 Let $\{\mu_{D_n}\}_{n \in \mathbb{N}}$ be a sequence of PDs such that $d_H(Z_{\mu_{D_n}^\omega}, Z_{\mu_D^\omega}) \rightarrow 0$, with $\omega : \mathbb{R}^2 \rightarrow \mathbb{R}$ being an effective weighting. Then $W_1(\mu_{D_n}, \mu_D) \rightarrow 0$.

Proof

By Theorem 1, we know that $d_H(Z_{\mu_{D_n}^\omega}, Z_{\mu_D^\omega}) \rightarrow 0$ implies $\mu_{D_n}^\omega \xrightarrow{w} \mu_D^\omega$ and that $\{\mu_{D_n}^\omega\}$ is uniformly integrable. We immediately have $\mu_{D_n}^\omega \xrightarrow{v} \mu_D^\omega$. We only need to check that $\text{Pers}(\mu_{D_n}) \rightarrow \text{Pers}(\mu_D)$.

Set $\mu_{D_n} = \sum_{p \in D_n} a_{n,p} \delta_p$.

By uniform integrability we have:

$$\lim_{r \rightarrow \infty} \sup_{n \in \mathbb{N}} \int_{B_r^c} \omega(p) \|p\|_2 d\mu_{D_n}(p) = \lim_{r \rightarrow \infty} \sup_{n \in \mathbb{N}} \int_{B_r^c} \|p\|_2 d\mu_{D_n}^\omega(p) = 0.$$

Since ω is an effective weight, this implies:

$$\lim_{r \rightarrow \infty} \sup_{n \in \mathbb{N}} \text{Pers}_{B_r^c}(\mu_{D_n}) \rightarrow 0,$$

For any $r \geq 0$ we can write:

$$\text{Pers}(\mu_{D_n}) = \int_{\mathbb{R}_{x < y}^2} (y - x) d\mu_{D_n}((x, y)) = \int_{B_r^c} (y - x) d\mu_{D_n}((x, y)) + \int_{B_r} (y - x) d\mu_{D_n}((x, y)).$$

Similarly, we can write:

$$\text{Pers}(\mu_D) = \int_{\mathbb{R}_{x < y}^2} (y - x) d\mu_D((x, y)) = \int_{B_r^c} (y - x) d\mu_D((x, y)) + \int_{B_r} (y - x) d\mu_D((x, y)).$$

If r is big enough, being D finite, we have $\text{supp}(D) \subset B_r$, and so $\int_{B_r^c} (y - x) d\mu_D((x, y)) = 0$ and $\int_{B_r} (y - x) d\mu_D((x, y)) = \text{Pers}(\mu_D)$.

Fix some r big enough so that the above holds. Since B_r is compact we can write a positive test function $g : \mathbb{R}_{x < y}^2 \rightarrow [0, 1]$ such that:

- g is continuous;

- $g \equiv 1$ on B_r ;
- $\text{supp}(g)$ is compact.

For such a g , we obtain:

$$0 \leq \int_{B_r} (y - x) d\mu_{D_n}((x, y)) \leq \int_{\mathbb{R}_{x < y}^2} g(x, y)(y - x) d\mu_{D_n}((x, y)).$$

Moreover, using vague convergence, we get:

$$\int_{\mathbb{R}_{x < y}^2} g(x, y)(y - x) d\mu_{D_n}((x, y)) \xrightarrow{n} \text{Pers}(\mu_D).$$

But:

$$\begin{aligned} \int_{\mathbb{R}_{x < y}^2} g(x, y)(y - x) d\mu_{D_n}((x, y)) &= \\ \int_{B_r} g(x, y)(y - x) d\mu_{D_n}((x, y)) + \int_{B_r^c} g(x, y)(y - x) d\mu_{D_n}((x, y)) &= \\ \int_{B_r} (y - x) d\mu_{D_n}((x, y)) + \int_{B_r^c} g(x, y)(y - x) d\mu_{D_n}((x, y)). \end{aligned}$$

Thus:

$$\begin{aligned} 0 \leq \int_{\mathbb{R}_{x < y}^2} g(x, y)(y - x) d\mu_{D_n}((x, y)) - \int_{B_r} (y - x) d\mu_{D_n}((x, y)) &= \\ \int_{B_r^c} g(x, y)(y - x) d\mu_{D_n}((x, y)) \leq \int_{B_r^c} (y - x) d\mu_{D_n}((x, y)). \end{aligned}$$

Putting the pieces together, for every $\varepsilon > 0$ there exist r_ε and N_ε such that, for every $n \geq N_\varepsilon$:

$$\begin{aligned} |\text{Pers}(\mu_{D_n}) - \int_{B_{r_\varepsilon}} (y - x) d\mu_{D_n}((x, y))| &\leq \varepsilon, \\ |\text{Pers}(\mu_D) - \int_{\mathbb{R}_{x < y}^2} g(x, y)(y - x) d\mu_{D_n}((x, y))| &\leq \varepsilon, \\ 0 \leq \int_{\mathbb{R}_{x < y}^2} g(x, y)(y - x) d\mu_{D_n}((x, y)) - \int_{B_{r_\varepsilon}} (y - x) d\mu_{D_n}((x, y)) &\leq \varepsilon, \end{aligned}$$

entailing $|\text{Pers}(\mu_{D_n}) - \text{Pers}(\mu_D)| \leq 3\varepsilon$, concluding the proof. ■